Original Article

In vivo evaluation of liver function by multimodal imaging in an alcohol-induced liver injury model

Xiao-Jing Song, Shu-You Wang, Shu-Yong Jia, Guang-Jun Wang, Wei-Bo Zhang

Department of Biomedical Engineering, Institute of Acupuncture & Moxibustion, China Academy of Chinese Medical Sciences, Beijing, China

Contributions: (I) Conception and design: XJ Song; (II) Administrative support: WB Zhang, GJ Wang; (III) Provision of study materials or patients: SY Wang, SY Jia; (IV) Collection and assembly of data: SY Wang, SY Jia; (V) Data analysis and interpretation: XJ Song, GJ Wang; (VI) Manuscript writing: All authors; (VII) Final approval of manuscript: All authors.

Correspondence to: Xiao-Jing Song, MD. Department of Biomedical Engineering, Institute of Acupuncture & Moxibustion, China Academy of Chinese Medical Sciences, 16 Nanxiao Street, Dongzhimennei, Dongcheng District, Beijing 100700, China. Email: xts2010@163.com; songxiaojing@mail.cintcm.ac.cn.

Background: Visually evaluating liver function is a hot topic in hepatology research. There are few reliable and practical visualization methods for evaluating the liver function *in vivo* in experimental studies. In this study, we established a multimodal imaging approach for *in vivo* liver function evaluation and compared healthy mice with chronic alcoholic liver injury (cALI) model mice to explore its potential applicability in experimental research.

Methods: In vivo fluorescence imaging (IVFI) technology was utilized to visually represent the clearance of indocyanine green from the liver of both healthy mice and mice with cALI. The reserve liver function was evaluated via IVFI using the Cy5.5-galactosylated polylysine probe, which targets the asialoglycoprotein receptor of hepatocytes. Hepatic microcirculation was assessed through laser speckle perfusion imaging of hepatic blood perfusion. The liver microstructure was then investigated by *in vivo* confocal laser endomicroscopy imaging. Finally, hepatic asialoglycoprotein receptor expression, histology, and the levels of serum alanine aminotransferase and aspartate aminotransferase were measured.

Results: *In vivo* multimodal imaging results intuitively and dynamically showed that indocyanine green clearance [mean ± standard deviation (SD): 30.83±14.71, 95% confidence interval (CI): 20.3 to 41.35], the fluorescence signal intensity (mean ± SD: 1,217.92±117.63; 95% CI: 1,148.38 to 1,290.84) and fluorescence aggregation area (mean ± SD: 5,855.80±1,271.81; 95% CI: 5,051.57 to 6,653.88) of Cy5.5-galactosylated polylysine targeting the asialoglycoprotein receptor, and hepatic blood perfusion (mean ± SD: 1,494.86±299.33; 95% CI: 1,316.98 to 1,690.16) in model mice were significantly lower than those in healthy mice (all P<0.001). Compared to healthy mice, the model mice exhibited a significant decline in liver asialoglycoprotein receptor expression (mean ± SD: 219.03±16.34; 95% CI: 208.97 to 230.69; P<0.001), increased serum alanine aminotransferase (mean ± SD: 149.70±47.89 U/L; 95% CI: 81.75 to 128.89; P=0.01) and aspartate aminotransferase levels (mean ± SD: 106.30±36.13 U/L; 95% CI: 122.01 to 180.17; P=0.021), hepatocyte swelling and deformation, disappearance of the hepatic cord structure, partial necrosis, and disintegration of hepatocytes. The imaging features of fluorescence signals in liver regions, hepatic blood perfusion and microstructure were biologically related to hepatic asialoglycoprotein receptor expression, serum indices of liver function, and histopathology in model mice.

Conclusions: Utilizing *in vivo* multimodal imaging technology to assess liver function is a viable approach for experimental research, providing dynamic and intuitive visual evaluations in a rapid manner.

Keywords: Multimodal imaging; in vivo fluorescence imaging (IVFI); laser speckle perfusion imaging (LSPI); *in vivo* confocal endomicroscopy imaging; liver function

Submitted Jan 31, 2023. Accepted for publication Jul 26, 2023. Published online Aug 10, 2023.
doi: 10.21037/qims-23-122
View this article at: https://dx.doi.org/10.21037/qims-23-122

Introduction

Various serum markers, liver biopsy, clearance and breath tests, and imaging are the primary methods used to assess liver function in clinical settings (1). Serum tests are indirect evaluations that cannot pinpoint the exact location of lesions and may also yield false negatives or false positives. Therefore, serum tests alone cannot diagnose liver diseases (2). Histopathological analyses of liver tissue require a sample, which may lead to metastasis and spread of malignant or infectious lesions and is not representative of the overall liver pathology and function (3). In animal studies, particularly of mice, liver function assessment requires the sacrifice of the animals, which is not suitable for the dynamic and long-term monitoring requirements of some studies. Clearance and breath tests are advantageous in that they can monitor the metabolic function of the liver in real time in a quantitative manner (4,5), but because of the influence of basal metabolic rate, smoking and other factors, these tests may not be reliable for qualitative or localized diagnosis of liver lesions. Thus, they may also not be well suited for experimental studies.

Compared to other methods, imaging allows for visualization of the location and nature of liver lesions and evaluation of liver function (6). Current imaging techniques commonly used for liver function evaluation include ultrasound, computed tomography (CT), magnetic resonance imaging (MRI), and positron-emission tomography (PET). Ultrasound and CT are the preferred noninvasive diagnostic methods for space-occupying liver lesions (7,8), although they are not accurate for qualitative diagnosis or liver function evaluation. MRI has high resolution and is suitable for qualitative diagnosis and liver function assessment (9), but it can be costly and relatively insensitive for experimental studies. PET is valuable in clinical tumor diagnosis and monitoring (10), but it is not effective for diagnosing liver injury from other causes. It has limitations in its ability to diagnose liver injury caused by nonvascular or non-space-occupying factors. While these imaging methods are valuable for diagnosing hepatic vascular or space-occupying lesions, it has limitations in accurately assessing and monitoring liver function for liver diseases, particularly in terms of localization and quantitative evaluation at the cellular and molecular levels. It would be beneficial to combine the advantages of imaging technologies to develop a multimodal *in vivo* imaging system suitable for evaluating *in vivo* liver function in experimental studies.

Based on the physiological and pathological characteristics of the liver, we used in vivo fluorescence imaging (IVFI), laser speckle perfusion imaging (LSPI), and *in vivo* probe confocal laser endomicroscopy (pCLE) technology to visually assess liver metabolism, reserve, microcirculation function, and histomorphology in mice with chronic alcoholic liver injury (cALI) and healthy mice. Due to the lower mortality and longer lifespan, Kunming mice were selected as models of alcoholic liver injury (11). By combining various imaging techniques, we establish a novel multimodal imaging method for liver function evaluation in liver lesion models, which has the potential to sensitively and visually characterize liver function in multiple dimensions *in vivo*. We investigate the feasibility of utilizing this innovative technique for experimental research on liver function evaluation. We present this article in accordance with the ARRIVE reporting checklist (available at https://qims.amegroups.com/article/view/10.21037/qims-23-122/rc).

Methods

Animals and groups

A total of 20 male Kunming mice, which were healthy adults that weighed 18–20 g, were enrolled in this study. The average age of these mice was 7 weeks. All animals were provided by Biotechnology Co., Ltd. [SCXK (Beijing) 2016-0002]. They were housed in sterilized isolation enclosures with a 12-hour alternating light-dark cycle and temperature kept at 21±2 ℃. The mice were given free access to a standard chow pellet diet and water. Experiments were performed under a project license (No. D2023-01-29-01) granted by the Animal Ethics Committee of the Institute of Acupuncture and Moxibustion at the China Academy of Chinese Medical Sciences in compliance with our institutional guidelines for the care and use of animals. All Kunming mice were numbered by another researcher, and the standard =RAND function in Microsoft Excel (Microsoft Corp., Redmond, WA, USA) was used to generate random numbers. Ten normal mice were randomly selected as the

control group (CG) (n=10); the remaining Kunming mice served as the cALI model group (MG) (n=10). The mice in the CG received all experimental treatments after 4 weeks of normal care. The mice in the MG were subjected to all experimental treatments after gavage with 50% ethanol [15 mL/kg body weight (BW)] daily for 4 weeks. According to the calculations of a previous study, the animal number in each group should be 10 (11). All experiments were performed according to the Guide for the Care and Use of Laboratory Animals.

Establishment of a cALI model

After 12 h of fasting, the mice were intragastric gavage with 50% ethanol (15 mL/kg BW) daily for 4 weeks. The model was counted as successful if the following conditions were met: (I) the liver became darker in color and harder in texture than a normal liver, or silt spots appeared on the surface of some liver tissues, and the relative weight of the liver increased; (II) serum alanine aminotransferase (ALT) and aspartate aminotransferase (AST) significantly increased; and (III) hematoxylin and eosin (H&E) staining showed that the structure of the liver cord had disappeared, the liver cells were enlarged, there were many fat droplets in the liver cells, and some hepatocytes showed signs of necrosis and disintegration by microscopy. Mice that died after oral administration or pathologically not meeting the above criteria were excluded from the experiment (12). All experiments were performed by the same individual to avoid the operator being a confounding variable.

IVFI of indocyanine green (ICG)

The mice were anesthetized under isoflurane (2% in oxygen) delivered via an anesthesia unit (Matrix Company, Midmark Animal Healthy, Versailles, OH, USA). After full anesthetization, the mice were injected via the tail vein with 10 μg/mL ICG solution (12.5 μL/g BW) (Suizhou Jiake Pharmaceutical and Chemical Industry Co., Ltd., Suizhou, Hubei, China) (n=10 per group, total animal number =20). Next, the mice were positioned prone in the recording chamber of an FX PRO multimodal *in vivo* imaging system (Carestream Health Inc., Woodbridge, CT 06525, USA) to stabilize the liver and fully expose it in the scanning window. The chamber was kept dark during the procedure. The instrumental parameters were set as follows: excitation wavelength, 790 nm; emission wavelength, 830 nm; and exposure time, 10 seconds. Images were acquired immediately after ICG injection and at 30 and 90 min under isoflurane anesthetization. The abdominal liver region of interest (ROI) was delineated through the identification of fluorescence signal areas by means of Carestream molecular imaging software (Carestream Health Inc., Woodbridge, CT 06525, USA). The fluorescence intensity (FI) in the liver regions at each specific time was analyzed using Carestream molecular imaging software. Two operators with more than 5 years of experience in IVFI performed all measurements independently. In addition, operator 1 performed a second imaging scan immediately after the initial examination, and operator 2 performed the imaging scan in the same manner, with no regard for the results of the first operator. The imaging results of operator 1 were used in statistical analyses. The operators were blinded to group information while doing the imaging and measuring the FI of liver ICG.

IVFI of Cy5.5-galactosylated polylysine (Cy5.5-GP) targeting hepatocyte asialoglycoprotein receptor (ASGPR)

Following ICG injection, the mice were injected via the tail vein with 0.005 μg/μL Cy5.5-GP solution (0.01 mL/g BW) (Beijing Hapten and Protein Biomedical Institute, Beijing, China) under inhalational isoflurane (1–2% in oxygen) (n=10 per group, total animal number =20). The mice were administered a Cy5.5-GP probe targeting hepatocyte ASGPR imaging. The instrumental parameters were set as follows: excitation wavelength, 630 nm; emission wavelength, 700 nm; and exposure time, 10 seconds. Images were acquired immediately and 60 min after Cy5.5-GP was injected via the tail vein. The ROI of the abdominal liver region was delineated through the identification of fluorescence signal areas by means of Carestream molecular imaging software (Carestream Health Inc., Woodbridge, CT 06525, USA). The FI and fluorescence aggregation area (FA) in the liver regions at each specific time were analyzed using Carestream molecular imaging software. In addition, operator 1 performed a second imaging immediately after the initial examination, and operator 2 performed the imaging in the same manner, with no regard to the results of the first operator. The imaging results of operator 1 were used in statistical analyses. The operators were blinded to group information.

LSPI of hepatic blood perfusion (HBP)

After IVFI, the mice (n=10 per group, total animal number =20) were deeply anesthetized with 20% urethane

[0.6 mL/100 g, Sigma-Aldrich (Shanghai) Trading Co., Ltd., Shanghai, China]. Once the mice were completely anesthetized and no movements were observed in the tail clamp for 1 min following the skin incision of the hind leg, the abdominal hair was shaved and the wall was disinfected. A minimally invasive opening was created below the rib margin on the left side. The lobe of the liver was exposed *in vivo* on the abdominal wall. The animals were incubated at a temperature of 30±0.5 ℃, and humidity levels were kept at 80–90%. This was done to minimize the impact of the surgery on HBP. HBP was detected using a Moor-FLPI perfusion imager (Moor Instruments, Axminster, Devon, UK; scanning area: 3 cm × 2 cm; pixel resolution: 576×768; image acquisition rate: 25 frames/s; 10-frame continuous acquisition mode; time interval: 1 s; and exposure time: 20 ms). The LSP images were scanned and analyzed using moorFLPI-V2.0 system software, and the average HBP of the liver surface was obtained (PU, the perfusion quantitative unit recorded within the Moor-FLPI system). Again, operator 1 performed a second imaging 5 min after the initial examination, and operator 2 performed the imaging in the same manner, with no regard to the results of the first operator. The imaging results of operator 1 were used in statistical analyses. The operators were blinded to group information.

In vivo pCLE of liver tissue morphology

After imaging of HBP, the exposed liver lobe was secured using a novel prototype apparatus to prevent respiratory disturbances (n=10 per group, total animal number =20). The liquid on the liver surface was wiped with a sterile cotton swab. Fluorescein isothiocyanate-dextran (FITC-dextran) (40,000 MW, Sigma Aldrich Co., St. Louis, MO 63103, USA) was washed off with 154 mM NaCl. The mice were injected via the tail vein with FITC-dextran solution (0.01 g/mL/kg BW). Then, Optiscan's FIVE2 (Optiscan Imaging Ltd., Melbourne, Australia) was applied to display and scan the images of hepatic histology (light source, 488 nm laser; excitation, 505–750 nm; laser power, 0–1,000 μW; scan depth, 0–400 μm; field of view, 464 μm ×261 μm). At 2 min after FITC-dextran injection, the scanning probe of the confocal endomicroscope equipment was vertically placed on the surface of liver tissue. The laser power and detection depth were adjusted to observe the morphological characteristics of liver tissues at different depths *in vivo*. Operator 1 performed a second imaging 15 min after the initial examination, and operator 2 performed the imaging in the same manner, with no regard to the results of the first operator. The imaging results of operator 1 were used in statistical analyses. The pCLE operators and the analyzers of hepatic histology images were blinded to group information.

Detection of serum markers of liver function

After confocal endomicroscopy imaging, the mice underwent cardiac blood sampling (n=10 per group, total animal number =20). The blood was centrifuged at 2,374 ×g at 4 ℃ for 10 min to obtain serum. Total levels of ALT and AST were detected using an Accute TBA-40FR automatic biochemical analyzer (Toshiba Medical System Co., Shimoishigami, Otawara-shi, Japan). The measurement was performed at least two times independently while blinded to group information.

Enzyme-linked immunosorbent assay (ELISA) and histological assessment

The mice were sacrificed by cervical dislocation after cardiac blood sampling, and then the liver tissues were removed quickly (n=10 per group, total animal number =20). Liver tissue (50 mg) was added to cold RIPA buffer (500 μL) and homogenized. The homogenate was centrifuged at 3,166 ×g at 4 ℃ for 20 min to obtain the supernatant. The total protein concentration in the supernatant was quantified by the bicinchoninic acid (BCA) assay (Thermo Pierce™ Rapid Gold BCA Protein Assay Kit, Thermo Scientific™, Waltham, MA, USA). The ASGPR content was determined using an ASGPR ELISA kit (JL3099X, Shanghai Jianglai Industrial Limited by Share, Ltd., Shanghai, China) following the manufacturer's protocol. A STAT FAX 2100 automatic microplate reader (Awareness Technology Inc., Palm City, FL, USA) was used for detection and analysis. The measurement was performed at least two times independently. A piece of liver tissue (1.0×0.5×0.2 cm^3) was cut and embedded in paraffin. Then, sections were sliced with a thickness of 6 μm, followed by conventional H&E staining. The structural and pathological changes in the liver tissue were observed by optical microscopy. All histopathological examinations were performed by pathologists with rich experience in liver pathological analysis while blinded to group information.

Statistical analysis

The Statistical Package for the Social Sciences (SPSS)

version 19.0 (SPSS Inc., Chicago, IL, USA) was used for statistical analysis. The mean FI and FA in each group were calculated. The mean levels of ALT and AST were calculated for each group. One-way analysis of variance (ANOVA) was used to compare indices between the groups, and the least significant difference (LSD) test for pairwise group comparisons was performed to detect significant differences (two-tailed P<0.05). The Jonckheere-Terpstra test was used for data that did not conform to a normal distribution. Data are expressed as the mean ± standard deviation (SD).

Results

Model establishment

Over the course of the experiment, we did not encounter any adverse events, and 10 Kunming mice under gavage with 50% ethanol were included in the experiment based on the blood biochemical index levels and hepatic histological features. In total, there were 20 mice included in this study.

IVFI of ICG in the liver

In both groups, after injecting ICG, fluorescence signals in the liver areas were observed within tens of seconds. At 30 min after injecting ICG, the FI reached its highest level and the FA was the largest. At 90 min after injecting ICG, the FI had significantly decreased, consistent with our previous results. IVFI showed that at 30 min after injecting ICG, the FI of the liver areas was higher in the CG than that in the MG, but at 90 min after injecting ICG, the FI of the liver areas was higher in the MG than that in the CG (*Figure 1A,1B*). Statistical analysis of the results showed that the rate of ICG clearance in the liver in the CG (mean ± SD: 69.19±11.55; 95% CI: 60.93 to 77.46) was significantly higher than that in the MG (mean ± SD: 30.83±14.71; 95% CI: 20.3 to 41.35; *Figure 1C*).

IVFI of Cy5.5-GP in the liver

IVFI showed that the FI in the liver areas of the two groups was comparable right after injecting Cy5.5-GP. At 60 min after injecting Cy5.5-GP, the FI of liver areas in the CG was stronger than that of the cALI MG (*Figure 2A*). Quantification of fluorescence signals in the liver areas *in vivo* showed that at 60 min after injecting Cy5.5-GP, the FI (mean ± SD: 1,757.58±97.12; 95% CI: 1,701.02 to 1,822.16) and FA (mean ± SD: 18,942.80±4,081.75; 95% CI: 16,685.98 to 21,304.49) of the liver areas in the CG were significantly higher than those in the MG (FI, mean ± SD: 1,217.92±117.63; 95% CI: 1,148.38 to 1,290.84, *Figure 2B*; FA, mean ± SD: 5,855.80±1,271.81; 95% CI: 5,051.57 to 6,653.88; *Figure 2C*). The fluorescence signal characteristics of Cy5.5-GP in the liver areas of each group at the final time point were contrary to those of ICG. ELISA showed that the ASGPR content of the liver in the MG (mean ± SD: 219.03±16.34; 95% CI: 208.97 to 230.69) was significantly lower than that in the CG (mean ± SD: 179.24±11.29; 95% CI: 173.02 to 185.91; *Figure 2D*).

Blood perfusion of the liver

Warm colors in LSP images indicate strong blood perfusion, cool colors weaker perfusion. Upon examination of the liver surface, red areas were present in the CG, signaling a high level of HBP. Conversely, the MG displayed light-green and yellow areas, indicating lower levels of HBP (*Figure 3A*). The quantification of HBP showed that the HBP of the CG (mean ± SD: 2,660.72±352.7; 95% CI: 2,435.6 to 2,868.88) was significantly higher than that of the MG (mean ± SD: 1,494.86±299.33; 95% CI: 1,316.98 to 1,690.16; *Figure 3B*).

Liver histology in vivo and in vitro

In the images of *in vivo* pCLE, the bright color in the field indicates liver cells, the dark color interstitial or intercellular space. In healthy mice, the hepatocytes exhibited regular size and shape and were arranged in well-ordered cords that formed radial patterns around small blood vessels. The hepatic sinusoid, which separates the hepatic cords, maintained a uniform space. In cALI mice, the hepatocytes appeared swollen, deformed, and disorganized, resulting in the destruction of the radial pattern of the hepatic cord. Some parts of the hepatic sinusoid were compressed and even vanished. Additionally, disintegrated hepatocytes were visible in certain areas, presenting no cell contours and being accompanied by dark tissues, indicative of necrotic regions (*Figure 4A*).

HE staining of liver tissue showed that the structure of the liver lobule of the healthy mice was intact, the size of the hepatocytes was uniform, and the hepatocytes were regularly arranged in a cord-like shape, radiating around the small blood vessels with the nuclei clearly visible in the center. Irregular liver sinusoids were seen between the liver cords, with a regular distribution. In the liver tissue of cALI mice,

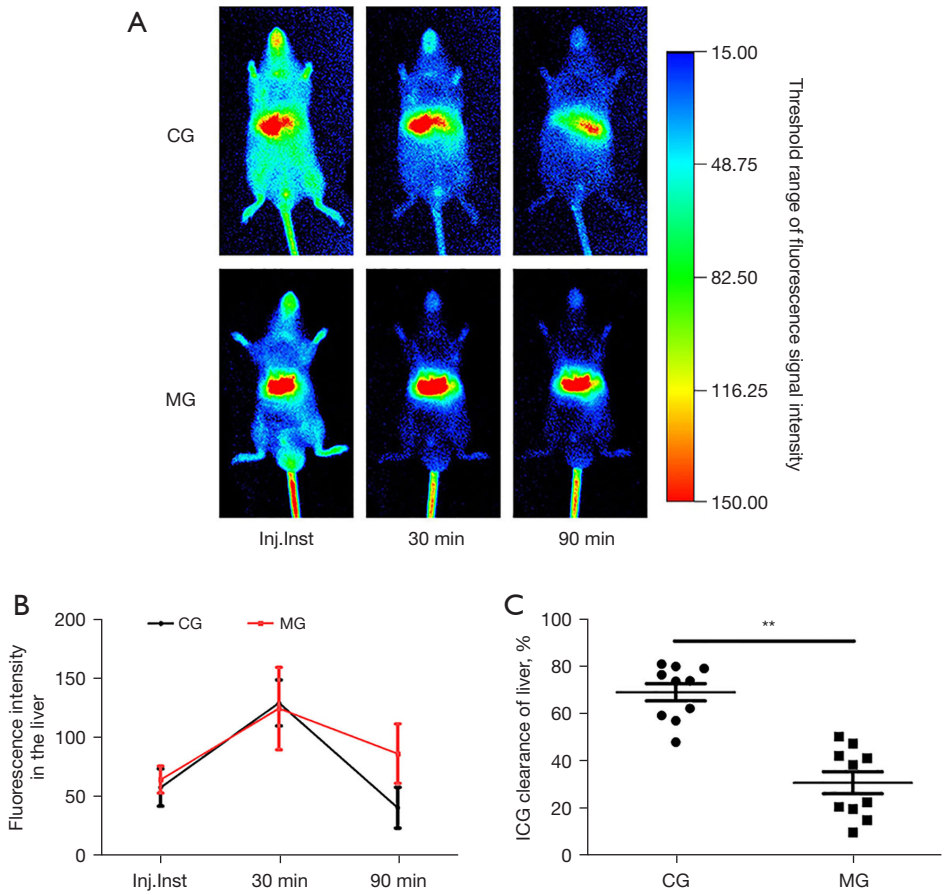

Figure 1 IVFI of ICG metabolism in the liver. (A) Visualization of liver ICG metabolism by IVFI (n=10). On IVFI, the red and bright-green areas in the middle of the mouse abdomen indicate ICG accumulation in the liver. The redder the color, the stronger the fluorescence signals and the more ICG in the liver. (B) Quantification of ICG fluorescence signal intensity in the liver (n=10). (C) Quantification of the ICG clearance rate in the two groups (n=10). The ICG clearance rate was calculated as the fluorescence intensity at 90 min minus the fluorescence intensity at 30 min divided by the fluorescence intensity at 30 min. Inj.Inst: immediately after ICG injection; 30 min: 30 min after ICG injection; 90 min: 90 min after ICG injection; CG: control group; MG: alcoholic liver injury model group. Data are mean ± standard deviation. **, P<0.01 *vs.* the CG (LSD two-group comparison test). IVFI, in vivo fluorescence imaging; ICG, indocyanine green; LSD, least significant difference.

the structure of the liver lobule was not there, the hepatocytes were enlarged, the cytoplasm was superficially stained, the hepatocytes were disordered, and some nuclei were not seen. Fat vacuoles of different sizes were seen in most hepatocytes, and a few liver cells were necrotic (*Figure 4B*).

Serum levels of ALT and AST

The level of ALT was significantly higher in the MG (mean ± SD: 149.70±47.89 U/L; 95% CI: 81.75 to 128.89) than the CG (mean ± SD: 37.10±6.67 U/L; 95% CI: 56.28 to 76.00; *Figure 4C*). The level of AST was also significantly higher in the MG (mean ± SD: 106.30±36.13 U/L; 95% CI: 122.01 to 180.17; CG: mean ± SD: 65.30±15.63 U/L; 95% CI: 33.29 to 41.09; *Figure 4D*).

Discussion

In clinical setting, the most common method for evaluating reserve liver function is the ICG excretion test. This test detects the ICG content in venous blood to calculate the retention rate 15 min after intravenous injection (13). Once injected, ICG is immediately distributed throughout the body via the blood circulation and is selectively

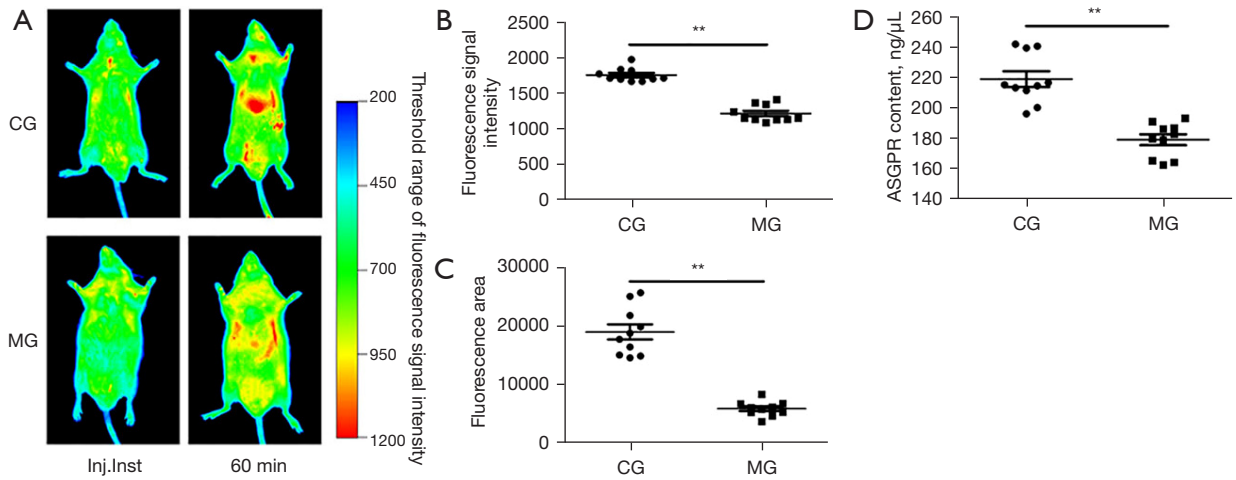

Figure 2 IVFI of ASGPR in the liver. (A) Visualization of Cy5.5-GP-targeted ASGPR by IVFI in the two groups (n=10). On IVFI, the red area in the middle of the mouse abdomen indicates Cy5.5-GP binding with hepatocyte ASGPR. The redder the color, the stronger the fluorescence signal and the greater the ASGPR expression in the liver. (B) Quantification of Cy5.5-GP fluorescence signal intensity in the liver (n=10). (C) Quantification of the Cy5.5-GP fluorescence aggregation area in the liver (n=10). (D) Densitometric analysis of ASGPR expression by ELISA (n=10). Inj.Inst: immediately after Cy5.5-GP injection; 60 min: 60 min after Cy5.5-GP injection; CG: control group; MG: alcoholic liver injury model group. **, P<0.01 *vs.* the CG (LSD two-group comparison test). Data are mean ± standard deviation. ASGPR, asialoglycoprotein receptor; Cy5.5-GP, Cy5.5-galactosylated polylysine; IVFI, in vivo fluorescence imaging; ELISA, enzyme-linked immunosorbent assay; LSD, least significant difference.

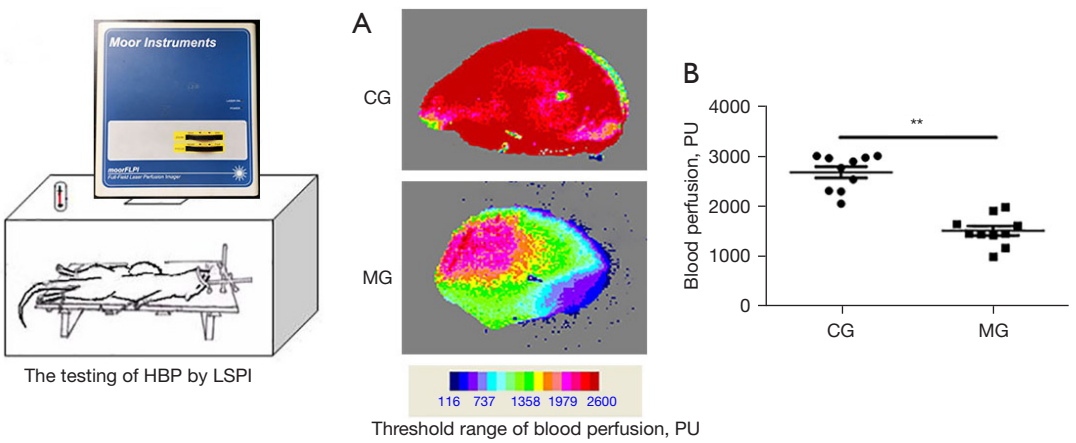

Figure 3 LSPI of the liver. (A) LSPI of the liver in healthy and cALI mice. On LSPI, the color range from cool to warm indicates low to high HBP. In the MG, more light-green and yellow areas were displayed on LSPI of the liver, indicating lower HBP. (B) Quantification of the mean HBP in the two groups (n=10). CG: control group; MG: cALI model group. Data are mean ± standard deviation. **, P<0.01 *vs.* the CG (LSD two-group comparison test). HBP, hepatic blood perfusion; LSPI, laser speckle perfusion imaging; cALI, chronic alcoholic liver injury; LSD, least significant difference.

absorbed by hepatocytes. The ICG typically reaches its highest concentration in blood approximately 30 min after injection. The liver clears ICG at a first-order rate and excretes it in a free form with the feces. When liver lesions form, the number of healthy hepatocytes decreases, and the clearance rate of ICG in the liver decreases significantly,

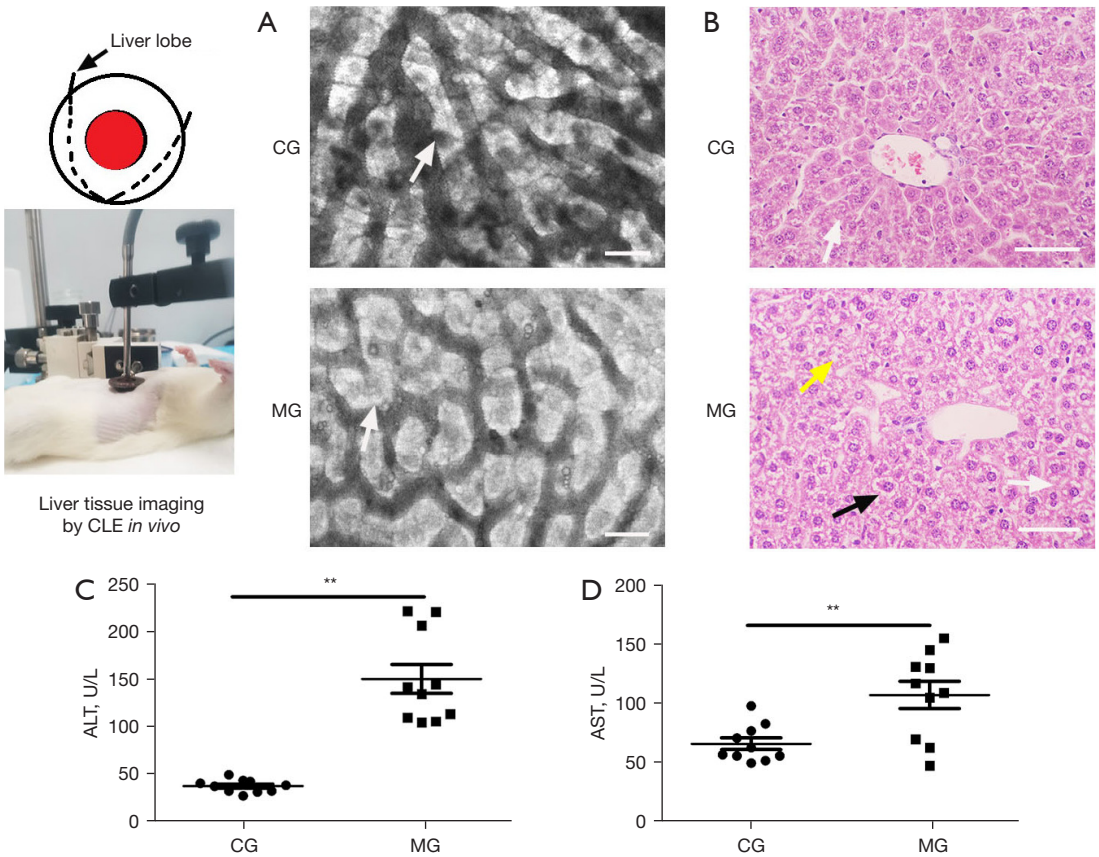

Figure 4 Comparison of hepatic histology and serum levels of liver function markers. (A) *In vivo* CLE images of liver tissue (×1,000), scale bar: 25 μm. In the CG image, the arrow indicates normal hepatocytes arranged in cords. In the MG image, the arrow indicates swollen and distended hepatocytes, with no hepatic cord structure. (B) H&E staining of liver tissue (×200), scale bar: 50 μm. The black arrow indicates steatotic hepatocytes, the yellow arrow indicates necrotic hepatocytes, and the white arrow indicates swollen and distended hepatocytes. (C,D) Comparison of ALT and AST levels between the two groups (n=10). CG: control group; MG: cALI model group. Data are mean ± standard deviation. **, P<0.01 *vs.* the CG (LSD two-group comparison test). CLE, confocal laser endomicroscopic; H&E, hematoxylin and eosin; ALT, alanine aminotransferase; AST, aspartate aminotransferase; cALI, chronic alcoholic liver injury; LSD, least significant difference.

prolonging the ICG retention in the liver (14,15). ICG is also a fluorescent complex of which FI is related to its tissue concentration. In this study, IVFI captured fluorescence signals from the liver region, displaying dynamic changes in ICG metabolism. The higher the FI and FA of a mouse liver region, the greater the ICG retention. The liver region of cALI mice showed significantly stronger FI after an ICG tail injection than that of healthy mice. This suggests substantial ICG retention in the liver regions of cALI mice, indicating fewer healthy hepatocytes and impaired liver function.

Cy5.5-GP-targeted imaging of ASGPR was carried out using IVFI technology. ASGPR is an important, highly efficient, specific receptor present on the surface of normal, as well as regenerated, human and mammalian hepatocytes (16). In a liver disease such as liver cancer, alcohol-related liver disease or hepatitis, ASGPR activity is impaired, and its expression is strongly downregulated. The ASGPR content is directly proportional to the degree of liver cell damage, so this can be used to evaluate liver function (17). Therefore, *in vivo* imaging methods that target ASGPR in hepatocytes can accurately determine the extent of hepatocyte damage in a sensitive and timely manner (11,18). In this study, after administering Cy5.5-GP through intravenous injection, Cy5.5-GP bound to ASGPR present on hepatocytes. Then, the fluorescence signals in the liver region were detected by IVFI. The FI and FA in a liver region represent the level of ASGPR expression.

The stronger the fluorescence signals, the greater the ASGPR expression, indicating the presence of more normal hepatocytes. In cALI mice, the fluorescence signal of Cy5.5-GP, targeting ASGPR, was significantly lower, this indicates the presence of more normal hepatocytes, resulting from in damaged liver function. This observation was also confirmed by the biochemical and histological results.

Typically, liver function assessment involves determining the liver ICG clearance rate and ASGPR content through blood or histological examination. However, in long-term experiments on animal models, frequent sampling can kill the animal. Particularly, sampling for multiple indicators may result in insufficient blood for testing in mice. Fortunately, IVFI is a noninvasive, highly sensitive, specific, uncomplicated method that does not involve radiation and is relatively cost-effective (19). IVFI has been used in protein and molecular expression research (20,21), tissue growth and metastasis analysis (22), organ function evaluation (17), and drug screening (23). Therefore, IVFI is an ideal choice for assessing liver function *in vivo*. IVFI visualization of liver ICG- and Cy5.5-GP-targeted ASGPR dynamically displayed the luminescent sites, and the ICG retention and ASGPR level of the liver *in vivo* were detected through the quantitative fluorescence signal of ICG and Cy5.5-GP in specific bands, which showed obvious differences between healthy mice and cALI mice. In addition, ICG and Cy 5.5-GP are fluorescent probes specifically for the liver. The emission wavelengths of Cy5.5-GP and ICG are in the red and near-infrared bands, respectively, and the noise from skin and other tissue is minimal. Therefore, their imaging depth can be up to 1 cm with high sensitivity and good specificity. In experimental studies, this is indeed a feasible and convenient method to evaluate liver function *in vivo*, but it is mainly used in rats and mice.

The liver is rich in blood vessels, and its physiology and pathology are closely related to its perfusion. Liver tissue lesions can lead to abnormal hemorheology of the liver (24). Under liver cirrhosis, hepatitis or fatty liver, liver perfusion is reduced (25,26). The hepatic microcirculation perfusion index is considered an important index for diagnosing liver diseases and evaluating liver function (27). Liver injury activates the coagulation system in the liver, resulting in disturbances in liver microcirculation, hepatocyte ischemia, and hypoxia. This is one of the pathological features of acute liver injury (ALI) (28). LSPI can detect the blood perfusion of tissues and organs at a depth of 2 mm and can be used to assess microcirculation. In this study, LSPI showed a lower HBP in cALI mice than healthy mice, suggesting liver dysfunction and microcirculation disturbance in cALI mice. Therefore, LSPI provides useful information for estimating liver function *in vivo* through HBP monitoring. However, HBP by LSPI is an indirect assessment of liver function and needs to be combined with other methods or indices for a comprehensive evaluation.

Histomorphology is commonly regarded as the standard diagnostic evaluation. As a result, this study utilized pCLE to visually display the microstructure of the liver *in vivo*. The conventional method of morphological examination typically entails taking samples and creating sections for observation (29). pCLE is a blend of confocal laser microscopy and traditional electronic endoscopy. Its probe can reach any organ or deep tissue with minimal invasion and carry out tomographic imaging of tissue at a specific depth, providing real-time and dynamic imaging of tissue microstructure, cellular, and molecular events *in vivo* (30). It has been utilized for high-resolution imaging of tissues, tracking molecules and microvasculature, and monitoring the metastasis of cancer cells (31-34). In this research, the cellular and tissue structures of various regions in the liver of healthy mice and those with cALI were dynamically visualized *in vivo* by pCLE. It displayed histopathological changes such as hepatocyte swelling and deformation, loss of hepatic cord architecture, and necrosis of certain hepatocytes in cALI mice *in vivo*, making them easily distinguishable from the healthy group. pCLE is significantly faster than traditional histopathological tests and offers flexible detection positioning to prevent omissions or mistakes in sampling. In comparison to traditional histopathological testing, pCLE provides a reliable reference for liver function evaluation through real-time and dynamic visualization of liver tissue structures. However, the detection depth of pCLE is limited to 400 μm, so deeper tissues must be assessed using alternative methods.

Multimodal imaging techniques, including IVFI of liver ICG, IVFI of Cy5.5-GP targeting ASGPR, LSPI of HBP, and pCLE imaging of liver tissues, have both advantages and disadvantages in experimental applications. We combined these imaging methods to comprehensively assess liver function. This multimodal imaging approach allowed for simultaneous monitoring of liver metabolism, hepatocyte reserve, blood perfusion, and microstructure in mice, providing visual data in digital form. The multilevel and multidimensional nature of this method enabled comprehensive characterization of liver function, from

protein expression and cell morphology to overall function. However, as liver disease pathologies vary, the multimodal imaging features used to assess liver function may differ among different liver diseases. In this study, the imaging findings of alcohol-induced steatohepatitis in model mice were obtained, but imaging characteristics of other liver disease models, such as mild alcoholic liver injury, alcoholic fibrosis and cirrhosis, drug-induced liver injury, herb-induced liver injury, nonalcoholic fatty liver disease, and hepatitis virus infection, were not observed. Therefore, this imaging method requires verification in models of various liver diseases and optimization of technical parameters to establish evaluation criteria for future experimental research.

Conclusions

The multimodal imaging approach that we applied to evaluate liver function *in vivo* enables dynamic and rapid visualization of changes in both the structure and function of the liver under both physiological and pathological conditions. This method provides extensive information on both the macroscopic and microscopic scales, ranging from organ function to protein expression. As a result, it can comprehensively reflect the degree of liver injury from multiple dimensions, providing reliable evidence for accurate liver function evaluation *in vivo*. Multimodal imaging for liver function assessment offers significant advantages and shows good prospects for use in experimental research, including drug development, liver disease diagnosis, treatment, and surgery.

Acknowledgments

We thank American Journal Experts (AJE) for providing English editing and Beijing Hapten and Protein Biomedical Institute for providing the fluorescence probe.
Funding: The research described in this paper was supported by the National Natural Science Foundation of China (NSFC) (Nos. 82274650 and 81704175).

Footnote

Reporting Checklist: The authors have completed the ARRIVE reporting checklist. Available at https://qims.amegroups.com/article/view/10.21037/qims-23-122/rc

Conflicts of Interest: All authors have completed the ICMJE uniform disclosure form (available at https://qims.amegroups.com/article/view/10.21037/qims-23-122/coif). The authors have no conflicts of interest to declare.

Ethics Statement: The authors are accountable for all aspects of the work in ensuring that questions related to the accuracy or integrity of any part of the work are appropriately investigated and resolved. Experiments were performed under a project license (No. D2023-01-29-01) granted by the Animal Ethics Committee of the Institute of Acupuncture and Moxibustion at the China Academy of Chinese Medical Sciences in compliance with our institutional guidelines for the care and use of animals.

References

1. Sharma P. Value of Liver Function Tests in Cirrhosis. J Clin Exp Hepatol 2022;12:948-64.
2. Sakka SG. Assessing liver function. Curr Opin Crit Care 2007;13:207-14.
3. Khalifa A, Rockey DC. The utility of liver biopsy in 2020. Curr Opin Gastroenterol 2020;36:184-91.
4. Sato N, Kenjo A, Suzushino S, Kimura T, Okada R, Ishigame T, Kofunato Y, Marubashi S. Predicting Post-Hepatectomy Liver Failure Using Intra-Operative Measurement of Indocyanine Green Clearance in Anatomical Hepatectomy. World J Surg 2021;45:3660-7.
5. Ferrandino G, Orf I, Smith R, Calcagno M, Thind AK, Debiram-Beecham I, Williams M, Gandelman O, de Saedeleer A, Kibble G, Lydon AM, Mayhew CA, Allsworth M, Boyle B, van der Schee MP, Allison M, Hoare M, Snowdon VK. Breath Biopsy Assessment of Liver Disease Using an Exogenous Volatile Organic Compound-Toward Improved Detection of Liver Impairment. Clin Transl Gastroenterol 2020;11:e00239.
6. Cruz M, Ferreira AA, Papanikolaou N, Banerjee R, Alves FC. New boundaries of liver imaging: from morphology to function. Eur J Intern Med 2020;79:12-22.

7. Hashimoto S, Hirooka Y, Kawabe N, Nakaoka K, Yoshioka K. Role of transabdominal ultrasonography in the diagnosis of pancreatic cystic lesions. J Med Ultrason (2001) 2020;47:389-99.
8. Jing M, Sun J, Xi H, Liu Z, Zhang S, Deng L, Han T, Zhang B, Lin X, Zhou J. Abdominal virtual non-contrast images derived from energy spectrum CT to evaluate chemotherapy-related fatty liver disease. Quant Imaging Med Surg 2023;13:669-81.
9. Kim JW, Lee CH, Yang Z, Kim BH, Lee YS, Kim KA. The spectrum of magnetic resonance imaging proton density fat fraction (MRI-PDFF), magnetic resonance spectroscopy (MRS), and two different histopathologic methods (artificial intelligence vs. pathologist) in quantifying hepatic steatosis. Quant Imaging Med Surg 2022;12:5251-62.
10. Sørensen M, Fode MM, Petersen JB, Holt MI, Høyer M. Effect of stereotactic body radiotherapy on regional metabolic liver function investigated in patients by dynamic [18F]FDGal PET/CT. Radiat Oncol 2021;16:192.
11. Song X, Wang S, Zhao C, Zhang W, Wang G, Jia S. Visual method for evaluating liver function: targeted in vivo fluorescence imaging of the asialoglycoprotein receptor. Biomed Opt Express 2019;10:5015-24.
12. Bertola A, Mathews S, Ki SH, Wang H, Gao B. Mouse model of chronic and binge ethanol feeding (the NIAAA model). Nat Protoc 2013;8:627-37.
13. Iimuro Y. ICG Clearance Test and 99mTc-GSA SPECT/CT Fusion Images. Visc Med 2017;33:449-54.
14. Cortese S, Peligros MI, Sola E, García-Alfonso P, Tellado JM. Indocyanine green clearance test as a predictor of chemotherapy liver toxicity and post-operative complications in patients with colorectal liver metastases. Cir Cir 2022;90:310-8.
15. Ibis C, Albayrak D, Sahiner T, Soytas Y, Gurtekin B, Sivrikoz N. Value of Preoperative Indocyanine Green Clearance Test for Predicting Post-Hepatectomy Liver Failure in Noncirrhotic Patients. Med Sci Monit 2017;23:4973-80.
16. Li Y, Yang CF, Zuo H, Li A, Das SK, Yu JH. Asialoglycoprotein Receptor-Targeted Superparamagnetic Perfluorooctylbromide Nanoparticles. Contrast Media Mol Imaging 2021;2021:5510071.
17. Sun R, Fang L, Lv X, Fang J, Wang Y, Chen D, Wang L, Chen J, Qi Y, Tang Z, Zhang J, Tian Y. In vitro and in vivo evaluation of self-assembled chitosan nanoparticles selectively overcoming hepatocellular carcinoma via asialoglycoprotein receptor. Drug Deliv 2021;28:2071-84.
18. Zhang D, Guo Z, Zhang P, Li Y, Su X, You L, Gao M, Liu C, Wu H, Zhang X. Simplified quantification method for in vivo SPECT/CT imaging of asialoglycoprotein receptor with (99m)Tc-p(VLA-co-VNI) to assess and stage hepatic fibrosis in mice. Sci Rep 2016;6:25377.
19. Liu N, Chen X, Kimm MA, Stechele M, Chen X, Zhang Z, Wildgruber M, Ma X. In vivo optical molecular imaging of inflammation and immunity. J Mol Med (Berl) 2021;99:1385-98.
20. Kim S, Lee S, Chang H, Kim M, Kim MJ, Kim KH. In vivo fluorescence imaging of conjunctival goblet cells. Sci Rep 2019;9:15457.
21. Wan X, Sun R, Bao Y, Zhang C, Wu Y, Gong Y. In Vivo Delivery of siRNAs Targeting EGFR and BRD4 Expression by Peptide-Modified Redox Responsive PEG-PEI Nanoparticles for the Treatment of Triple-Negative Breast Cancer. Mol Pharm 2021;18:3990-8.
22. You J, Pan C, Park K, Li A, Du C. In vivo detection of tumor boundary using ultrahigh-resolution optical coherence angiography and fluorescence imaging. J Biophotonics 2020;13:e201960091.
23. Liu F, Zhang P, Liu Z, Song F, Ma C, Sun Y, Feng Y, He Y, Zhang G. In vivo accurate detection of the liver tumor with pharmacokinetic parametric images from dynamic fluorescence molecular tomography. J Biomed Opt 2022;27:070501.
24. Yang L, Cao H, Sun D, Hou B, Lin L, Shen ZY, Song HL. Bone marrow mesenchymal stem cells combine with normothermic machine perfusion to improve rat donor liver quality-the important role of hepatic microcirculation in donation after circulatory death. Cell Tissue Res 2020;381:239-54.
25. Gracia-Sancho J, Marrone G, Fernández-Iglesias A. Hepatic microcirculation and mechanisms of portal hypertension. Nat Rev Gastroenterol Hepatol 2019;16:221-34.
26. Ozaki K, Kozaka K, Kosaka Y, Kimura H, Gabata T. Morphometric changes and imaging findings of diffuse liver disease in relation to intrahepatic hemodynamics. Jpn J Radiol 2020;38:833-52.
27. Takahashi H, Shigefuku R, Yoshida Y, Ikeda H, Matsunaga K, Matsumoto N, Okuse C, Sase S, Itoh F, Suzuki M. Correlation between hepatic blood flow and liver function in alcoholic liver cirrhosis. World J Gastroenterol 2014;20:17065-74.
28. Magdaleno F, Blajszczak CC, Nieto N. Key Events Participating in the Pathogenesis of Alcoholic Liver Disease. Biomolecules 2017;7:9.

29. Kulkarni N, Masciola A, Nishant A, Kim KJ, Choi H, Gmitro A, Freeman EE, Semeere A, Nakalembe M, Kang D. Low-cost, chromatic confocal endomicroscope for cellular imaging in vivo. Biomed Opt Express 2021;12:5629-43.
30. Vaculová J, Kroupa R, Kala Z, Dolina J, Grolich T, Vlažný J, Said D, Izakovičová Hollá L, Bořilová Linhartová P, Procházka V, Joukal M, Jabandžiev P, Slabý O, Kunovský L. The Use of Confocal Laser Endomicroscopy in Diagnosing Barrett's Esophagus and Esophageal Adenocarcinoma. Diagnostics (Basel) 2022;12:1616.
31. Ramani RS, Tan I, Bussau L, Angel CM, McCullough M, Yap T. Confocal microscopy in oral cancer and oral potentially malignant disorders: A systematic review. Oral Dis 2022. [Epub ahead of print]. doi: 10.1111/odi.14291.
32. Chen H, Liu L, Qian K, Liu H, Wang Z, Gao F, Qu C, Dai W, Lin D, Chen K, Liu H, Cheng Z. Bioinspired large Stokes shift small molecular dyes for biomedical fluorescence imaging. Sci Adv 2022;8:eabo3289.
33. Acerbi F, Pollo B, De Laurentis C, Restelli F, Falco J, Vetrano IG, Broggi M, Schiariti M, Tramacere I, Ferroli P, DiMeco F. Ex Vivo Fluorescein-Assisted Confocal Laser Endomicroscopy (CONVIVO® System) in Patients With Glioblastoma: Results From a Prospective Study. Front Oncol 2020;10:606574.
34. Vargas G, Vincent KL, Zhu Y, Szafron D, Brown TC, Villarreal PP, Bourne N, Milligan GN, Motamedi M. In Vivo Rectal Mucosal Barrier Function Imaging in a Large-Animal Model by Using Confocal Endomicroscopy: Implications for Injury Assessment and Use in HIV Prevention Studies. Antimicrob Agents Chemother 2016;60:4600-9.

Cite this article as: Song XJ, Wang SY, Jia SY, Wang GJ, Zhang WB. *In vivo* evaluation of liver function by multimodal imaging in an alcohol-induced liver injury model. Quant Imaging Med Surg 2023;13(10):6434-6445. doi: 10.21037/qims-23-122

